S17

Supporting Information for *Why are Mountaintops Cold? The Transition of Surface Lapse Rate on Dry Planets*

Bowen Fan[1], Malte F. Jansen[1], Michael A. Mischna[2], Edwin S. Kite[1]

[1]Department of the Geophysical Sciences, University of Chicago, Chicago, IL, 60637, USA

[2]Jet Propulsion Laboratory, California Institute of Technology, Pasadena, CA, 91109, USA

Contents of this file

Appendix A Simulations with a pure CO_2 atmosphere

To validate our GCM results against earlier work on early Mars (Forget et al., 2013; Wordsworth, 2016), we carried out simulations with a pure CO_2 atmosphere using a correlated-k scheme (Mischna et al., 2012). The settings are the same as with the gray gas simulations (see Section 2), except for the radiation scheme. The surface pressure, p_s (equivalent to p_{CO2}), is varied from 0.01 bar to 3 bar. We also performed a set of simulations with modern Mars topography.

We find similar transitions in surface temperature, T_s, distribution (Fig. S1a & Fig. S1b) and surface lapse rate, γ (Fig. S1c), as in the gray gas runs. The value of γ is close to 100% for a thick CO_2 atmosphere (which has both a high surface pressure and high optical thickness), and converges to 0 for a thin CO_2 atmosphere (which has low surface pressure and low optical thickness). Quantitatively, our simulations are consistent with Fig. 7 in Forget et al. (2013) in

that $\gamma \approx 100\%$ for $p_s = 3$ bar, and $\gamma \approx 80\%$ for $p_s = 1$ bar. The slope of γ does not depend on topography (compare the blue line and red line in Fig. S1c). We also find that only with the correlated-k CO_2 scheme, the upper limit of γ exceeds 90%, while for the gray gas scheme,

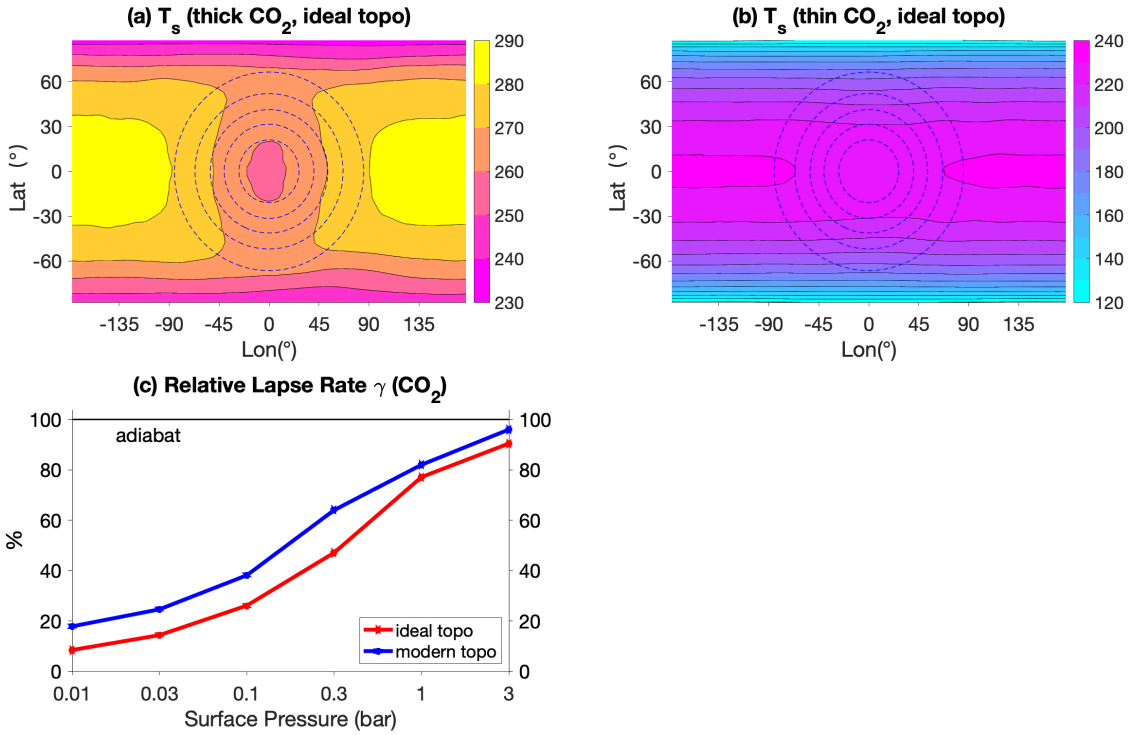

Figure S1. Example of annual mean surface temperature, T_s, patterns and relative surface lapse rates (γ) under CO_2 atmospheres. (a) Surface temperature (filled contours) for surface pressure $p_s = 3$ bar. The ideal topography is plotted in blue dashed lines with a contour interval of 1000 m from 1000 m to 5000 m. (b) Same as (a), but with $p_s = 0.01$ bar. (c) The transition of γ with p_s. The data is sampled on a logarithmic grid with $p_s = 0.01, 0.03, 0.1, 0.3, 1, 3$ bar. Red solid (ideal topo): obliquity equals zero, no atmospheric condensation, default idealized topography, sensible heat flux enabled. Blue solid (modern topo): same as ideal topo, but with modern Mars topography.

we have not obtained values of γ above 80% (Fig. 1). The cause for this difference between a gray gas and and CO_2 atmosphere is beyond the scope of this investigation (see the discussion in Section 4).

Appendix B Role of off-equatorial topography and off-equatorial latitude band

To test the sensitivity to the choice of latitudinal band, we check the lapse rate transition with a shifted idealized topography and latitudinal band.

Fig. S2 shows the data with a gray gas scheme and a revised Gaussian topography. Fig. S2(a) shows the topography (black line) and indicates the latitudinal band used for averaging: 30°N−50°N

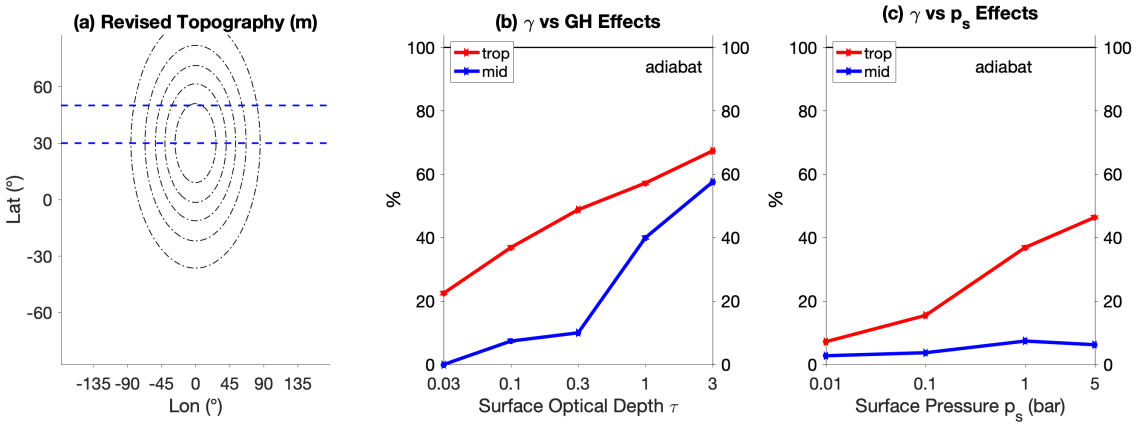

Figure S2. (a) Revised Gaussian topography. The shape is the same as the original Gaussian topography, but the center of the mountain is shifted to 30° N. The latitudinal band for sampling data is shown in blue dashed lines. (b) The transition of surface lapse rate, γ, with τ, for $p_s = 1$ bar. Red line (trop): simulations focused on the tropics, with the original Gaussian topography and data sampled from the tropical band. Blue line (mid): simulations focused on mid-latitudes, with the revised topography and mid-latitudinal band. (c) Same as (b), but for $\tau = 0.1$ and varied p_s.

(blue line). Fig. S2(b)&(c) compares the transition of relative surface lapse rate, γ, between the default cases with tropical topography and tropical band (red line, also see Fig. 1) and the revised topography and mid-latitude band. We find γ still increases with τ, but γ is much smaller when the atmosphere is optically thin ($\tau < 1$ for Fig. S2b, also in Fig. S2c). This is because the troposphere gains heat by advection from low latitudes in those cases ($F_H < 0$, see Section 3.3), which stabilizes (i.e., reduces) the atmospheric lapse rate. Importantly, we also find the mid-latitude lapse rate to be essentially independent of p_s. This result is consistent with the argument from Section 3.3 that an increase in atmospheric heat flux divergence (out of the tropics) with increasing p_s is the key for the tropical surface lapse rate change.

Appendix C The near-surface atmospheric pattern of limiting cases

Fig. S3 shows the typical patterns of near-surface atmospheric temperature, T_a, and horizontal winds. T_a follows closely with T_s (Fig. 1), with minor modulation by the winds across the elevated topography (Wordsworth et al., 2015).

Appendix D Full surface energy budgets for gray gas simulations

The energy budgets for all default gray gas simulations are shown in Fig. S4.

Appendix E Two-column model

This section includes the choice of parameters and the results for the two-column model. The parameters are listed in the table below.

The topography-related variables are calculated by spatially averaging the values within the highland box and lowland box, respectively. Here we define the highland area to include all elevations higher than the half-height of the idealized mountain ($Z_s > 3000$ m). This leads to a

highland surface fraction within the tropical belt, α, of 0.3056. Then $Z_{s,HL}$, $Z_{s,LL}$, $p_{s,HL}$, $p_{s,LL}$ are calculated by spatial averaging over the respective regions. The calculation of the atmospheric energy budget requires an additional assumption on the atmospheric level. Here we choose the atmospheric pressure $p_c = 0.4p_s$. At this level, the atmosphere above the highlands and lowlands has reached a weak temperature gradient in all our GCM simulations (Fig. S5). Then the thickness of the atmospheric layer above highland H_a is calculated as:

$$H_a = H\frac{log\,(p_{s,HL})}{log\,(p_c)} \tag{E1}$$

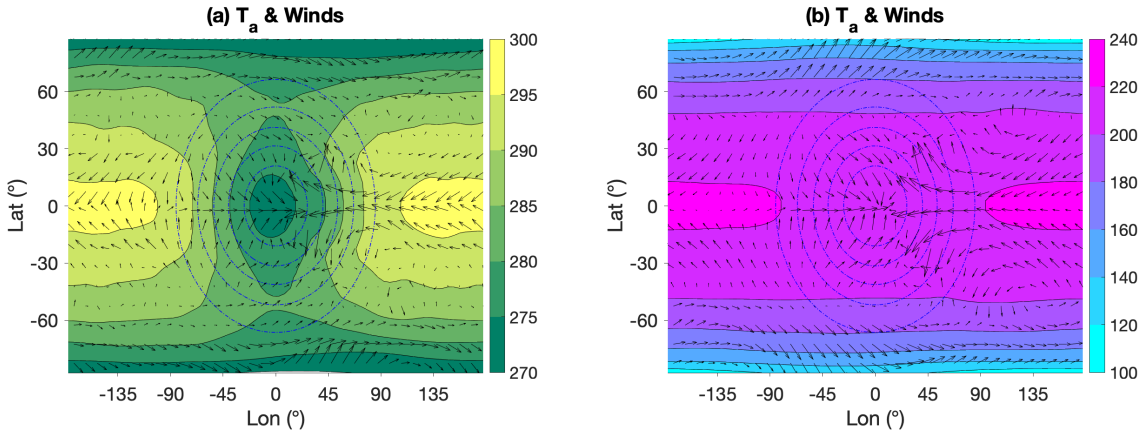

Figure S3. Example of annual mean near-surface temperature patterns under different atmospheres. (a) Near-surface atmospheric temperature T_a (filled contours) and near-surface wind speeds for surface pressure $p_s = 5$ bar and global mean surface optical depth $\tau = 5$. The maximum zonal wind speed is 3.4 m/s and the maximum meridional wind speed is 2.5 m/s. (b) Same as (a), but for the case with $p_s = 0.01$ bar and $\tau = 0.01$. The maximum zonal wind speed is 10.3 m/s and the maximum meridional wind speed is 8.1 m/s.

where $H = \frac{RT_{s,HL}}{g}$ is the scale height. The altitude of the atmosphere is calculated as $Z_a = H_a + Z_{s,HL}$.

An advective cooling term, F_H, is included in the atmospheric equations (Eq. 10&11) because the Hadley circulation transports heat from the tropics to higher latitudes. For each simulation, F_H is calculated by spatially averaging the top of atmosphere (TOA) radiative imbalance within the tropical atmospheric band:

$$F_H = \overline{LW_{\downarrow,TOA} + SW_{\downarrow,TOA} - LW_{\uparrow,TOA} - SW_{\uparrow,TOA}} \tag{E2}$$

where the overbar denotes a horizontal average, upward arrows represent fluxes that go into space, and downward arrows represent fluxes that enter the atmosphere.

After plugging in the parameters, we numerically solve the model equations for the temperature and energy fluxes. The surface lapse rate from the two-column model is defined as:

$$\gamma_{two-column\ model} = -\frac{1}{\Gamma_a}\frac{T_{s,HL} - T_{s,LL}}{Z_{s,HL} - Z_{s,LL}} \times 100\% \tag{E3}$$

Table S1. Parameters from GCM outputs

Table S1.

insolation SW (W/m^2)	137.84								
gravity g (m/s^2)	3.7								
highland fraction α	0.3056								
highland elevation $Z_{s,HL}$ (m)	4873								
lowland elevation $Z_{s,LL}$ (m)	754								
optical depth τ	0.1				1	0.3	0.03	0.01	0.003
surface pressure p_s (Pa)	5.08E5	1.02E5	1.03E4	1200	1.02E5				
highland pressure $p_{s,HL}$ (Pa)	3.79E5	7.60E4	7.68E3	890	7.60E4				
lowland pressure $p_{s,LL}$ (Pa)	5.48E5	1.10E5	1.11E4	1290	1.10E5				
advective cooling F_H (W/m^2)	9.6400	6.5528	4.5974	2.6564	12.0747	9.3281	4.5974	2.6564	1.8889

References

Forget, F., et al. (2013). 3D modelling of the early Martian climate under a denser CO_2 atmosphere: Temperatures and CO_2 ice clouds. *Icarus*, *222*(1), 81–99.

Mischna, M. A., Lee, C., & Richardson, M. (2012). Development of a fast, accurate radiative transfer model for the Martian atmosphere, past and present. *Journal of Geophysical Research (Planets)*, *117*(E10), E10009.

Wordsworth, R. D. (2016). The climate of early Mars. *Annual Review of Earth and Planetary Sciences*, *44*(1), 381-408.

Wordsworth, R. D., Kerber, L., Pierrehumbert, R. T., Forget, F., & Head, J. W. (2015). Comparison of "warm and wet" and "cold and icy" scenarios for early Mars in a 3-D climate

74 model. *Journal of Geophysical Research: Planets*, *120*(6), 1201–1219.

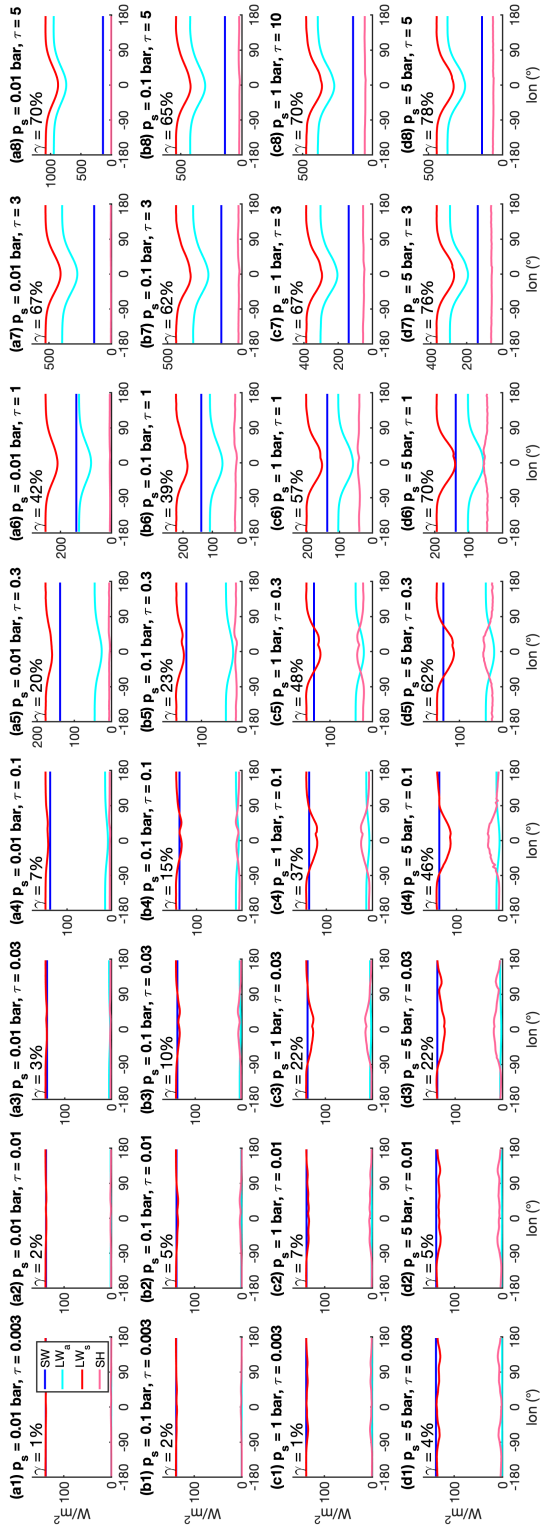

Figure S4. Time-averaged surface energy budgets for all cases shown in Fig. 1c.

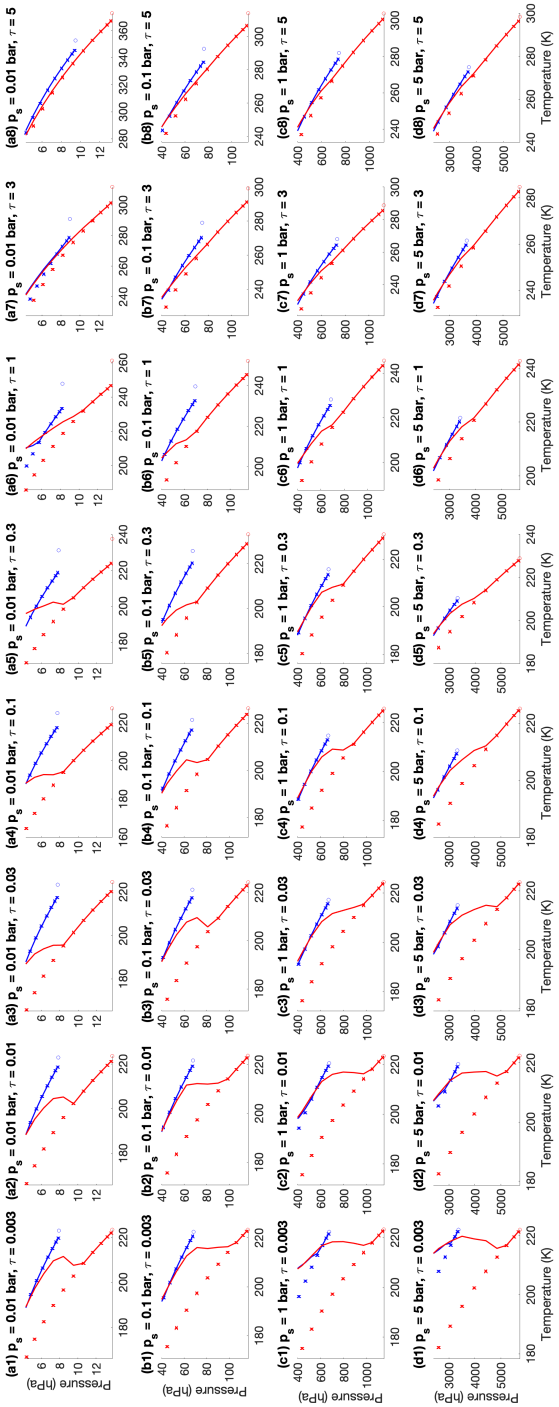

Figure S5. Time-averaged vertical thermal structure above the equatorial highlands (blue, lon = 0°) and lowlands (red, lon = 180°) for all cases shown in Fig. 1c. Circles, solid lines, and crosses correspond to surface temperature, atmospheric temperature, and adiabats, respectively.

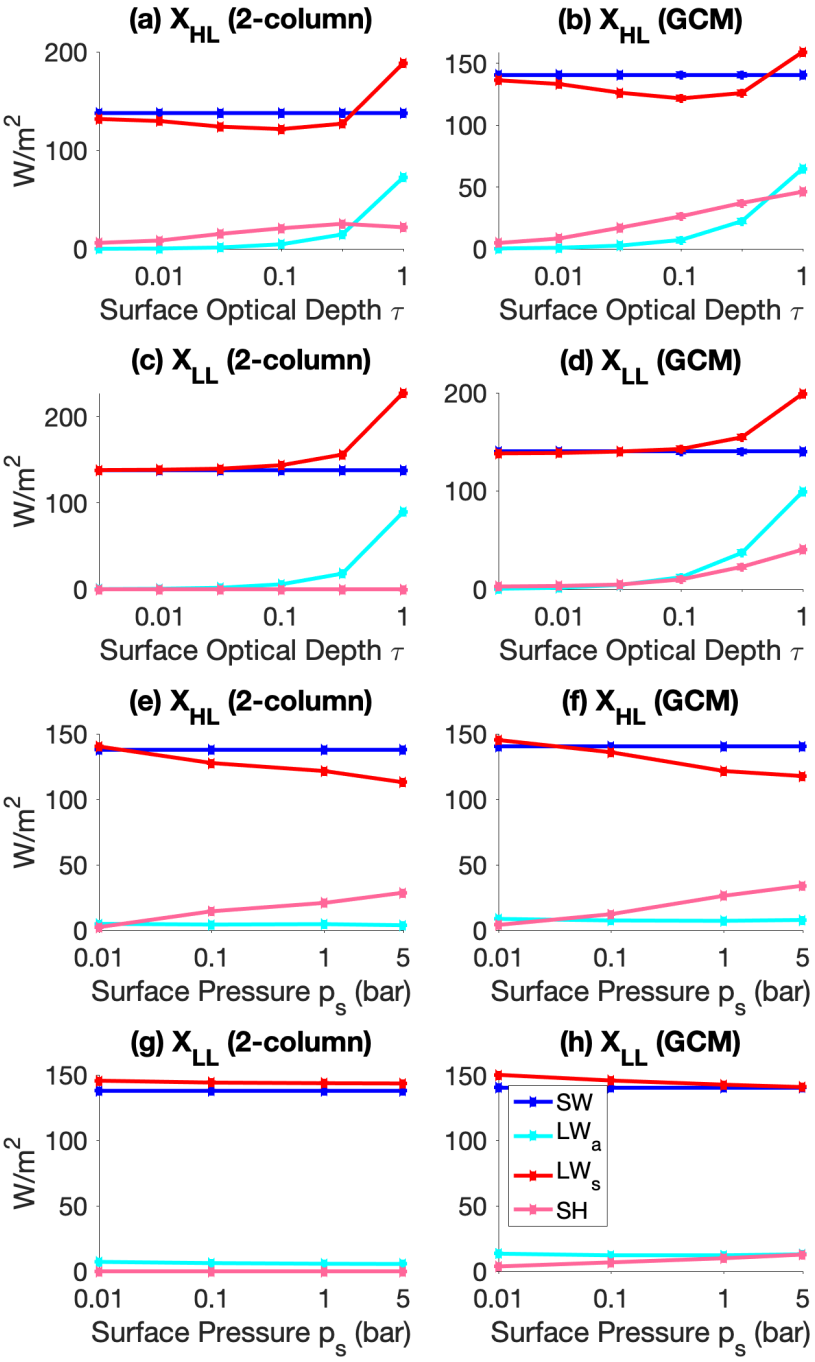

Figure S6. (a) Surface energy budget components in the highland column of the two-column model with $p_s = 1$ bar. (b) Same as (a), but for the GCM. (c) Same as (a) but for the lowland column. (d) Same as (c), but for the GCM. (e, f, g, h) Same as the top rows, but for the cases with $\tau = 0.1$ and varied p_s.